


Cite this: *J. Mater. Chem. C*, 2018,
6, 369Charge carrier trapping processes in lanthanide
doped LaPO_4 , GdPO_4 , YPO_4 , and LuPO_4 †Tianshuai Lyu * and Pieter Dorenbos

Various methods for deliberate design of electron and hole trapping materials were explored with a study on double lanthanide doped rare earth ortho phosphates. Cerium acts as a recombination center, while lanthanide codopants act as electron trapping centers in $\text{LaPO}_4:0.005\text{Ce}^{3+},0.005\text{Ln}^{3+}$. The electron trap depth generated by lanthanide codopants can be tailored by the choice of lanthanide, and for a fixed set of lanthanide dopants like in $\text{Gd}_{1-x}\text{La}_x\text{PO}_4:0.005\text{Ce}^{3+},0.005\text{Ho}^{3+}$ solid solutions, by changing x , leading to conduction band (CB) engineering. Herein, the electrons liberated from Ho^{2+} recombined through the conduction band at Ce^{4+} to yield Ce^{3+} 5d–4f emission. In contrast, samarium, europium and ytterbium act as recombination centers, while Tb^{3+} and Pr^{3+} act as hole trapping centers in double lanthanide doped YPO_4 , as Tb^{3+} and Pr^{3+} codopant recombination is realized *via* hole release rather than the more commonly reported electron release. The holes recombine *via* the valence band with the electrons trapped in Yb^{2+} , Sm^{2+} , or Eu^{2+} to generate 4f–4f luminescence from Yb^{3+} , Sm^{3+} , or Eu^{3+} . Lu^{3+} was introduced in YPO_4 to tailor the valence band (VB) energy and to tune the hole trap depths of Tb^{3+} and Pr^{3+} in $\text{Y}_{1-x}\text{Lu}_x\text{PO}_4:0.005\text{Ln}^{3+}$ solid solutions. Our results shed light on the deliberate design of electron and hole trapping materials based on a deep understanding of trap level locations and on the transport and trapping processes of charge carriers.

Received 15th November 2017,
Accepted 6th December 2017

DOI: 10.1039/c7tc05221a

rsc.li/materials-c

1. Introduction

The trapping and release processes of charge carriers are of interest for practical applications and from a theoretical point of view.^{1,2} When electron and hole trapping materials are exposed to high energy radiation, for instance, beta radiation or ultraviolet (UV) light, free electron and hole charge carriers are generated and then trapped in trapping centers, which are usually lattice defects or impurities.³ The trapped holes or electrons can be released by optical, thermal, or mechanical excitation, ultimately yielding photon emission at wavelengths that can range from ultraviolet to infrared, depending on the recombination centers and type of compound.^{1,4} For storage phosphors applied in X-ray imaging, deep traps (~ 2 eV) are needed to avoid thermal fading at room temperature (RT).⁵ Relatively shallow traps ($< \sim 0.7$ eV) are required to generate RT afterglow.^{6,7} So, if we can control the trap depth of holes or electrons, then in principle one can engineer or tune storage and afterglow properties.

The electron trapping and release processes have been widely investigated.^{1,8–11} Ueda *et al.* reported the valence change of Ce^{3+}

and Cr^{3+} in $\text{Y}_3\text{Al}_2\text{Ga}_3\text{O}_{12}$ persistent phosphors using X-ray absorption near edge structure (XANES) spectroscopy.¹² Concentration of both Ce^{4+} and Cr^{2+} increases after exposure to UV light. This shows that Ce^{3+} is the electron donor and the electrons produced *via* photoionization can be trapped by Cr^{3+} electron trapping centers. By thermal excitation at room temperature, the electrons trapped at Cr^{2+} are liberated slowly to the conduction band and then recombine with Ce^{4+} to finally generate Ce^{3+} emission peaked at ~ 510 nm.¹³ A similar partial oxidation of Eu^{2+} to Eu^{3+} after UV light excitation is observed in the well-known persistent phosphor $\text{SrAl}_2\text{O}_4:\text{Eu}^{2+},\text{Dy}^{3+}$ using XANES.¹⁴

Holes can also be liberated to recombine with a luminescence center. Hole transport can occur *via* a migrating V_k center or through the valence band.² Such hole trapping and release processes are scarcely reported. One of the few reports was by Chakrabarti *et al.* in the 1980s; they observed that cerium acts as a hole trapping center and samarium as a recombination center in $\text{MgS}:\text{Ce}^{3+},\text{Sm}^{3+}$ after UV light excitation.¹⁵ Holes are liberated from Ce^{4+} earlier than electrons from Sm^{2+} and recombine with Sm^{2+} , generating Sm^{3+} 4f–4f emission. The other two examples are from studies by Luo *et al.* on $\text{Gd}_{1-x}\text{La}_x\text{AlO}_3$ ⁷ and $\text{RE}_2\text{O}_2\text{S}$.² The trap depth of the Tb^{3+} hole trapping center in $\text{Gd}_{1-x}\text{La}_x\text{AlO}_3$ can be adjusted by changing x , leading to valence band energy changes. In $\text{RE}_2\text{O}_2\text{S}:\text{Ti}^{4+}$, a hole release process leading to Ti^{4+} charge transfer emission is identified.

Delft University of Technology, Faculty of Applied Sciences, Department of Radiation Science and Technology, Section Luminescence Materials, Mekelweg 15, 2629JB Delft, The Netherlands. E-mail: T.lyu-1@tudelft.nl

† Electronic supplementary information (ESI) available. See DOI: 10.1039/c7tc05221a

The scarce research on hole trapping and release processes is associated with a lack of knowledge on how to distinguish a hole trapping process from an electron trapping process. For that, we need information on where the hole or electron traps are located within the bandgap. It was not until 2012 that the chemical shift model was published, which enables one to create a vacuum referred binding energy (VRBE) diagram. One may now compare the binding energy at the valence band top or conduction band bottom in various compounds with respect to the same reference energy.^{16–19} This model shows that the VRBE in the $4f^n$ ground state of trivalent and divalent lanthanides is almost independent of the type of compound.^{20–23} Consequently, lanthanide related hole trap depth can be tuned by altering the VRBE at the top of the valence band and electron trap depth can be tuned through tailoring of the VRBE at the bottom of the conduction band.⁷

In this paper, based on constructed VRBE diagrams and band gap engineering, we show how to deliberately design storage phosphors through precisely controlling the release of electrons and of holes. La, Gd, Y, and Lu phosphates are selected as hosts due to their simple structures with only one site to substitute for a trivalent lanthanide. To demonstrate the design concept, the constructed VRBE diagram of YPO_4 is already shown in Fig. 1. The zigzag curves I and II link the VRBE of an electron in the ground states of divalent and trivalent lanthanides, respectively. Such a diagram is very useful to decide which shallow and deep electron–hole trap combinations can be used to arrive at specific properties. For example, Eu^{3+} 4f–4f emission is observed for the Eu^{3+} – Tb^{3+} pair in YPO_4 after hole release from Tb^{4+} , since it is predicted that Eu^{3+} acts as a much deeper electron trap than Tb^{3+} does as a hole trap.

Fig. 2 shows the stacked VRBE diagram for the four REPO_4 compounds studied in this work. It shows that the lanthanide trap depth can be engineered by changing the VRBE at the conduction band bottom or valence band top. For instance, the hole trap depth of Pr^{3+} or Tb^{3+} can be decreased by replacing Lu^{3+} by Y^{3+} , Gd^{3+} , or La^{3+} .

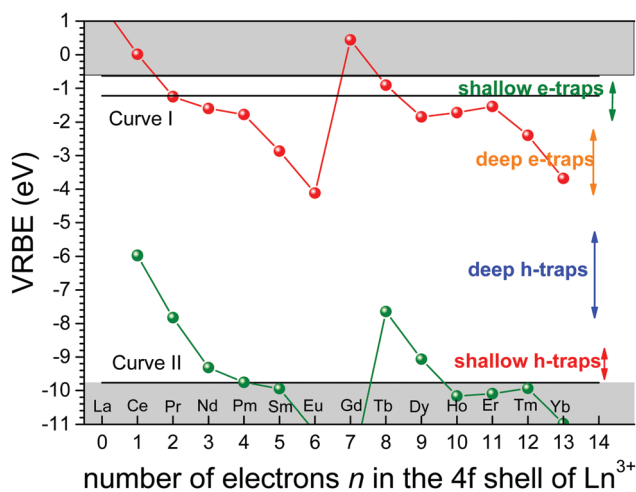


Fig. 1 Vacuum referred binding energy (VRBE) diagram of YPO_4 with various Ln traps.

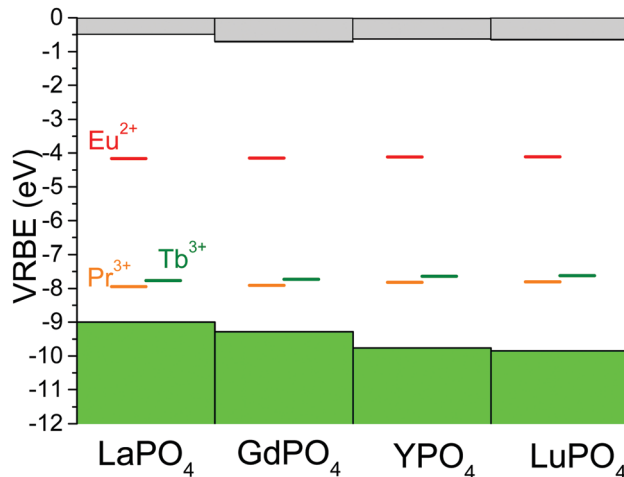


Fig. 2 Stacked VRBE diagram of REPO_4 with the binding energy in the ground states of Eu^{2+} , Pr^{3+} , and Tb^{3+} .

2. Experimental

All starting chemicals were purchased from Sigma-Aldrich and used without further treatment. Polycrystals were fabricated by a high temperature solid-state reaction. The appropriate stoichiometric mixture of $\text{NH}_4\text{H}_2\text{PO}_4$ (99.99%), La_2O_3 (99.99%), Gd_2O_3 (99.99%), Y_2O_3 (99.99%), Lu_2O_3 (99.999%) and other rare earth oxides (99.999%) were accurately weighted and mixed well in agate mortar with the help of acetone. The concentrations of the other rare earth oxides were fixed at 0.5 mol%. Afterwards, the mixture was fired in an alumina crucible for 10 h at $1400\text{ }^\circ\text{C}$ under a reducing atmosphere of H_2/N_2 ($\text{H}_2:\text{N}_2$ 7% : 93%). After cooling, the as-synthesized polycrystals were ground again and fired at $1400\text{ }^\circ\text{C}$ for another 10 h under the same reducing atmosphere. Finally, the polycrystals were naturally cooled to room temperature, and the obtained compounds were ground into a powder before subjecting them to further measurements.

The crystal structures were characterized by a PANalytical XPert PRO X-ray diffraction system with cobalt $\text{K}\alpha$ ($\lambda = 0.1788901\text{ nm}$) X-ray tube at 40 mA and 45 kV. The collected X-ray diffraction (XRD) patterns were compared with the reference data derived from Pearson's Crystal Database. The photoluminescence emission (PL) and PL excitation (PLE) spectra were recorded with equipment that has a UV/Vis branch with a 500 W Hamamatsu CW xenon lamp and Horiba Gemini 180 monochromator, and the VUV/UV branch consisted of an ARC VM502 vacuum monochromator and a deuterium lamp (D_2 lamp). Princeton Instruments Acton SP 2300 monochromator and PerkinElmer Photon Counting Module MP1993 were used to disperse and record the emission from the samples. The sample temperature was controlled with a closed-cycle helium (He) cryostat (Model HC-4, APD Cryogenics Inc.) and a temperature controller of Lake Shore 331. All presented excitation curves were corrected for the incident photon flux.

Thermoluminescence (TL) measurements were recorded utilizing a RISØ TL/OSL reader (model DA-15) with DA-20 controller. All samples were irradiated with a $^{90}\text{Sr}/^{90}\text{Y}$ β source

with a dose rate of 0.7 mGy s^{-1} in the TL setup in complete darkness. All TL measurements were performed under a flow of nitrogen gas. Samples with masses $<20 \text{ mg}$ and area $\sim 0.6 \text{ cm}^2$ were used. For the TL measurements on samples where Ce^{3+} was the recombination center, a 3 mm Hoya C5-58 filter in the wavelength range of 350–470 nm was placed between the EMI 9635QA photomultiplier tube (PMT) and the sample to record Ce^{3+} emission only. In order to select the red emission when, for example, Eu^{3+} was the recombination center, a 600 nm bandpass filter of 600FS40-50 (S250-07) was placed between the PMT and sample.

For the low temperature TL (LTTL) measurements (90–450 K), the samples were first heated to 450 K for 2 min to empty all relevant traps and then cooled to 90 K followed by 600 s β irradiation with a $^{90}\text{Sr}/^{90}\text{Y}$ β source at a dose rate of 0.4 mGy s^{-1} . LTTL recordings were measured at a heating rate of 1 K s^{-1} in a sample chamber operating under vacuum (10^{-7} mbar), monitoring Eu^{3+} red emission with a PerkinElmer channel photomultiplier tube (MP-1393). Liquid nitrogen was utilized as the cooling medium.

Prior to the recording the TL emission (TLEM) spectra, the samples were heated to 900 K 3 times to empty all relevant traps and then exposed to γ -ray irradiation from a ^{60}Co source to charge the traps. Emission was recorded with a UV/vis spectrometer (Ocean Optics, model QE65000) in the 200–900 nm range and a near-infrared (NIR) spectrometer (Ocean Optics, model NIRQ512) in the 900–1700 nm range. Both spectrometers had a high-resolution composite grating of 300 lines per mm and an 100 mm entrance aperture, leading to wavelength resolution of full width at half maximum (FWHM) of 3.3 nm.

TL excitation (TLE) spectra were recorded by first illuminating samples for 2400 s using a monochromatic photon beam from a 150 W xenon lamp (Hamamatsu L2273) filtered by a monochromator (Oriol Cornerstone 130). The system was operated under Labview™, allowing the collection of multiple TL glow curves from room temperature to 720 K at heating rate of 5 K s^{-1} with changing illumination wavelength. The wavelength step was 10 nm, and the slit width was set at 0.1 cm, resulting in a spectrum resolution of 8 nm. The plot of the integrated TL glow curve versus the excitation wavelength was called the TL excitation spectrum.²⁴ To collect Eu^{3+} emission, a 600 nm bandpass filter of 600FS40-50 was placed between the PMT and the samples.

3. Results

3.1. X-ray diffraction and photoluminescence spectroscopy

Fig. 3 shows part of the XRD patterns of $\text{Gd}_{1-x}\text{La}_x\text{PO}_4:0.005\text{-Ce}^{3+},0.005\text{Ho}^{3+}$ ($x = 0\text{--}1$) solid solutions. GdPO_4 and LaPO_4 have the same crystal structure as the space group $P12_1/c1$. Compared to pure GdPO_4 , the diffraction peaks showed a slight shift towards smaller 2θ angles because the lanthanum ions entered into the smaller gadolinium sites and increased the cell volume. Similar solid solutions were prepared for $\text{Y}_{1-x}\text{Lu}_x\text{PO}_4:0.005\text{Eu}^{3+},0.005\text{Tb}^{3+}$ and the XRD patterns shown

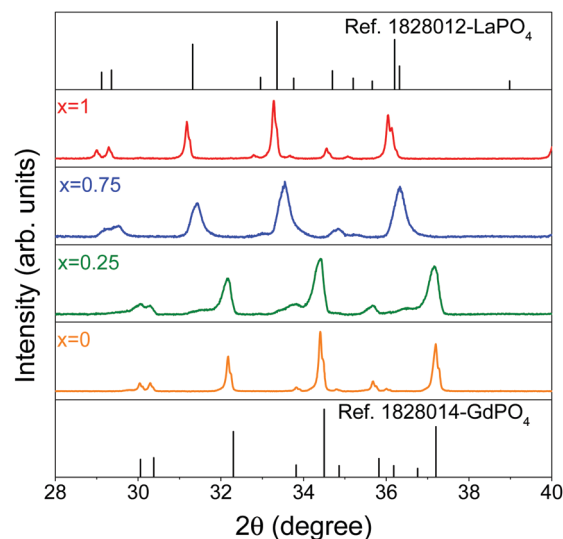


Fig. 3 XRD patterns in the range from 28° to 40° for $\text{Gd}_{1-x}\text{La}_x\text{PO}_4:0.005\text{-Ce}^{3+},0.005\text{Ho}^{3+}$ solid solutions.

in Fig. S1, ESI† agree with those obtained by in Levushkina *et al.*²⁵

Fig. 4 shows the VUV excitation spectra of 590 nm Eu^{3+} emission in $\text{REPO}_4:0.005\text{Eu}^{3+},0.005\text{Tb}^{3+}$ at 10 K. The shortest wavelength peak was due to host exciton creation. Its energy E^{ex} increased from 8.05 eV for LaPO_4 to 8.67 eV for LuPO_4 , which agrees with previous reports, *i.e.*, 8.00 eV for LaPO_4 ²² and 8.60 eV for LuPO_4 .²⁶

The broad excitation bands near 200–260 nm were due to electron transfer from the valence band to Eu^{3+} and are known as the charge transfer (CT) bands. The energy E^{CT} at the maximum of the CT band increased from 4.88 eV for LaPO_4 to 5.76 eV for LuPO_4 . These CT-energies are similar to those in literature: 4.84 eV for LaPO_4 and 5.74 eV for LuPO_4 .^{22,27}

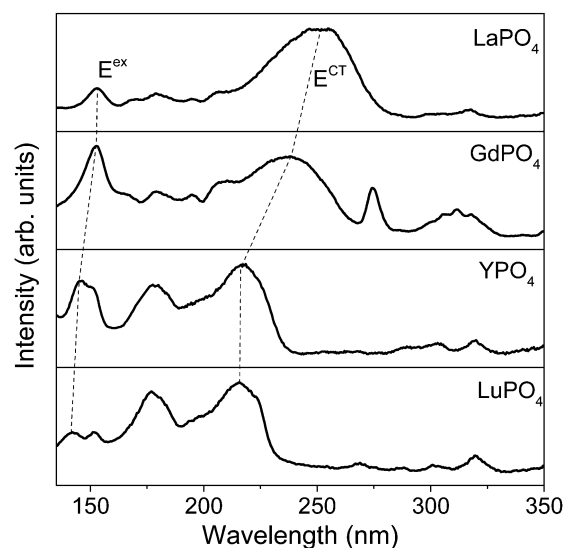


Fig. 4 Photoluminescence excitation (PLE) spectra ($\lambda_{\text{em}} = 590 \text{ nm}$) of $\text{REPO}_4:0.005\text{Eu}^{3+},0.005\text{Tb}^{3+}$ (RE = La, Gd, Y, and Lu) samples at 10 K.

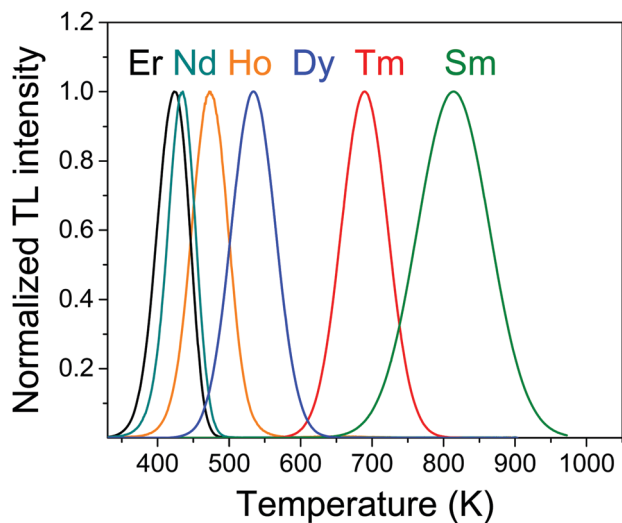


Fig. 5 Normalized TL glow curves of $\text{LaPO}_4:0.005\text{Ce}^{3+},0.005\text{Ln}^{3+}$ at heating rate $\beta = 5 \text{ K s}^{-1}$ while monitoring the Ce^{3+} 5d–4f emission.

3.2. Engineering the electron trap depth

A series of $\text{LaPO}_4:0.005\text{Ce}^{3+},0.005\text{Ln}^{3+}$ samples were prepared to demonstrate electron trap depth engineering. All samples were of single phase, as demonstrated in the XRD spectra of Fig. S1, ESI.† Fig. 5 shows the normalized TL glow curves. Each of the Ln^{3+} codopants induced a TL glow at different temperatures T_m as listed in column 2 of Table 1.

Assuming first-order TL-recombination kinetics, the trap depth can be determined from a variable heating rate plot using the relation^{28–31}

$$\ln\left(\frac{T_m^2}{\beta}\right) = \frac{E}{kT_m} + \ln\left(\frac{E}{ks}\right) \quad (1)$$

where β is the heating rate (K s^{-1}), k is the Boltzmann constant (eV K^{-1}), and s is the frequency factor (s^{-1}). Fig. 6 shows the variable heating rate plot for $\text{LaPO}_4:0.005\text{Ce}^{3+},0.005\text{Er}^{3+}$. For the trap depth, a value of 1.05 eV was obtained from the slope of the line through the data and a frequency factor value of $1.02 \times 10^{12} \text{ s}^{-1}$ was obtained from the intercept with the vertical axis. Since all Ln^{3+} codopants were located at the La^{3+} sites, we assumed that the frequency factor s remained constant.^{7,32} The trap depths for the codopant other than Er^{3+} were determined by using T_m from column 2 of Table 1 and solving eqn (1) with $\beta = 5 \text{ K s}^{-1}$. The trap depths are shown in column 3 of Table 1.

Table 1 TL results on $\text{LaPO}_4:0.005\text{Ce}^{3+},0.005\text{Ln}^{3+}$ showing T_m (K) and the trap depths E (eV) derived from the variable heating rate plot

Ln	T_m	E
Nd	434	1.08
Sm	817	2.07
Dy	535	1.34
Ho	474	1.18
Er	424	1.05
T_m	690	1.74

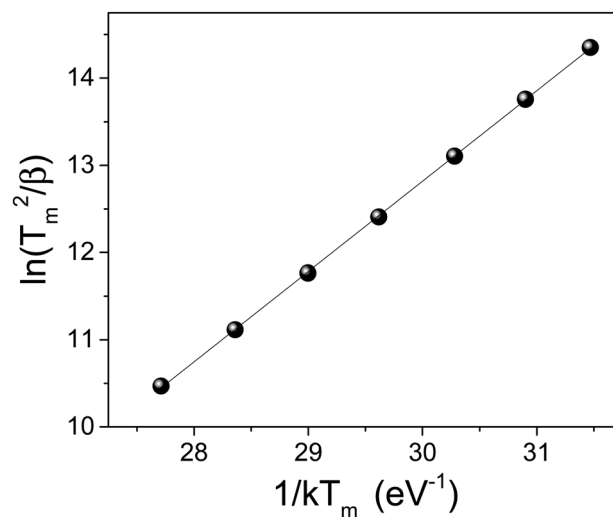


Fig. 6 Variable heating rate plot of $\text{LaPO}_4:0.005\text{Ce}^{3+},0.005\text{Er}^{3+}$. The used heating rates were 0.08, 0.15, 0.30, 0.63, 1.25, 2.5, and 5 K s^{-1} .

Fig. 7a shows the normalized TL glow curves for $\text{Gd}_{1-x}\text{La}_x\text{PO}_4:0.005\text{Ce}^{3+},0.005\text{Ho}^{3+}$ solid solutions. T_m gradually shifted towards higher temperature with increasing x . The TL glow peak for $x = 0.25$ was the broadest. From variable heating rate plot fitting for $x = 0, 0.5, 0.75$, and 1, as can be found in Fig. S2, ESI,† the trap depths and frequency factors that are compiled in Table 2 were derived.

To study the glow peak broadening of the sample with $x = 0.25$, we applied the peak cleaning technique.³³ After exposure to the β source for 200 s at room temperature, the sample was heated to a different peak clean temperature (T_{clean}) and maintained at that temperature for 400 s. Subsequently, TL measurements at a heating rate of 5 K s^{-1} were recorded. Fig. 7b shows that with an increase in T_{clean} , the TL intensity decreased and T_m increased. This showed the presence of a trap depth distribution for the sample with $x = 0.25$, and the increase in T_m was due to the fact that the electrons trapped in the shallow traps were liberated at T_{clean} and only the deeper traps remained occupied. The trap depth against T_{clean} could be found by using the initial rise method, as explained in the supplementary information in Fig. S3, ESI.† The trap depth varied between 0.9 and 1.2 eV, as shown column 3 of Table 2. Also, for $x = 0.5$ and 0.75, there peak broadening related to trap depth distribution was observed and the energies in column 3 of Table 2 were regarded as the average trap depth.

3.3. Engineering hole release in Y-Lu phosphate solid solutions

Fig. 8 shows the TL emission (TLEM) plots for $\text{YPO}_4:0.005\text{Eu}^{3+},0.005\text{Tb}^{3+}$, $\text{YPO}_4:0.005\text{Sm}^{3+},0.005\text{Tb}^{3+}$, $\text{YPO}_4:0.005\text{Yb}^{3+},0.005\text{Tb}^{3+}$, and $\text{YPO}_4:0.005\text{Yb}^{3+}$. Additional TL emission plots for other REPO_4 with other combinations of Ln^{3+} doping can be found in Fig. S4, ESI.†

The glow peak at $\sim 507 \text{ K}$ for $\text{YPO}_4:0.005\text{Eu}^{3+},0.005\text{Tb}^{3+}$, which will be referred to as peak IIIa, was also observed for $\text{YPO}_4:0.005\text{Sm}^{3+},0.005\text{Tb}^{3+}$ in Fig. 8b and $\text{YPO}_4:0.005\text{Yb}^{3+},0.005\text{Tb}^{3+}$

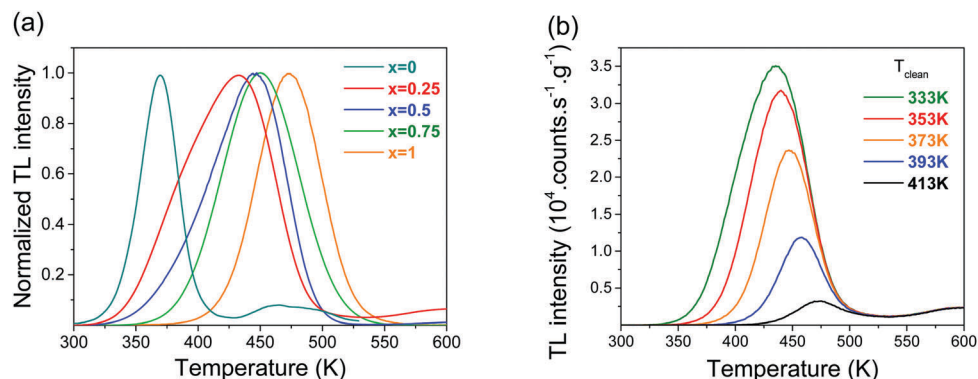


Fig. 7 (a) Normalized TL glow curves of $Gd_{1-x}La_xPO_4:0.005Ce^{3+},0.005Ho^{3+}$ solid solutions at $\beta = 5 \text{ K s}^{-1}$. (b) TL glow curves for $x = 0.25$ after a peak cleaning at T_{clean} .

Table 2 TL results on $Gd_{1-x}La_xPO_4:0.005Ce^{3+},0.005Ho^{3+}$ solid solutions listing the T_m (K), trap depth E (eV), and frequency factor s (s^{-1}) as obtained from variable heating rate plots. The data for $x = 0.25$ is from the peak cleaning and the initial rise method

x	T_m	E	s
0	369	0.84	9.53×10^{10}
0.25	432	0.95–1.20	
0.5	445	1.10	3.58×10^{12}
0.75	451	1.16	2.51×10^{12}
1	474	1.22	2.95×10^{12}

in Fig. 8c. From the studies by Bos *et al.*³⁵ on $YPO_4:0.005Sm^{3+},0.005Tb^{3+}$ and $YPO_4:0.005Tm^{3+},0.005Tb^{3+}$, this glow peak was attributed to hole release from Tb^{4+} . Note that characteristic luminescence originating from Tb^{3+} is absent in Fig. 8 but characteristic emission from either Eu^{3+} , Sm^{3+} , or Yb^{3+} is observed. This applies to YPO_4 and equally well to other $REPO_4$ in Fig. S4, ESI.†

The effect of replacing Tb^{3+} for Pr^{3+} or Ce^{3+} is shown in the TL glow curves of Fig. 9a and b. Information on TLEM can be found in Fig. S4, ESI.† Pr^{3+} gave a glow peak, hereafter referred to as peak IIIb, that is at 10 K lower temperature than peak IIIa for Tb^{3+} . The glow peak was absent when Ce^{3+} was the co-dopant or in case of absence of co-dopants. The VRBE diagram of Fig. 1 predicted that Tb^{3+} and Pr^{3+} provided about the same hole trapping depth and therefore peak IIIb was attributed to hole release from Pr^{4+} . From the variable heating rate plot of $YPO_4:Eu^{3+},Tb^{3+}$, we derived a frequency factor of $1.45 \times 10^{13} \text{ s}^{-1}$ for hole release from Tb^{4+} . We assumed that the same value applied for hole release from Pr^{4+} , and then by using the observed T_m in Fig. 9 and eqn (1), trap depths were derived as shown in Table 3.

Glow peak I occurred despite different sets of lanthanide dopants present in all TL-spectra of Fig. 9a and b. Its origin was not lanthanide related. We attributed it to hole release from unknown defects. The same applied to glow peaks II and IV that are present when Eu^{3+} was used as the deep electron trap.

Fig. 10 shows the TL glow curves for $Y_{1-x}Lu_xPO_4:0.005Eu^{3+},0.005Tb^{3+}$ solid solutions. With increasing x , peak IIIa shifted from 507 towards 572 K. The trapping parameters were derived using the variable heating rate plots¹³ in Fig. S6, ESI,† and the results were compiled in Table 3. TL glow curves for

$Y_{1-x}Lu_xPO_4:0.005Eu^{3+},0.005Pr^{3+}$ solid solutions could be found in Fig. S7, ESI.† Like peak IIIa for Tb^{3+} , peak IIIb for Pr^{3+} shifted from 494 towards 560 K with increasing x . The derived trapping parameters are shown in Table 3.

Fig. 11 compares the TL glow curves of $LuPO_4:0.005Eu^{3+},0.005Ln^{3+}$. Similar to that in Fig. 9, the glow peak IIIb for hole release from Pr^{4+} appeared at about 10 K lower temperature than that from Tb^{4+} and glow peaks I and IV were present. The TL glow curves of the single Eu^{3+} and Eu^{3+},Ce^{3+} -codoped samples were shown to demonstrate the absence of peaks IIIa and IIIb.

Fig. 12 shows the low temperature TL (LTTL) glow curves of $LaPO_4:0.005Eu^{3+},0.005Ln^{3+}$. Similar to that in Fig. 9 and 11, Pr gave rise to an additional glow peak below RT denoted as IIIb and Tb^{3+} to a glow peak IIIa at about 30 K higher temperature. The TL glow curve of the $LaPO_4:Eu^{3+},Ce^{3+}$ was shown to demonstrate the absence of peaks IIIa and IIIb. The glow peaks appearing above room temperature were further studied with a Riso reader, as shown in Fig. S8, ESI.† The variable heating rate plot for glow peak IIIa of $LaPO_4:0.005Eu^{3+},0.005Tb^{3+}$, as shown in Fig. S8b, ESI,† provided the trapping parameters. By assuming a similar frequency factor for glow peaks IIIa and IIIb, the activation energies compiled in Table 3 were estimated.

Because of the intense glow peaks near room temperature in the $LaPO_4$ samples, we measured the room-temperature isothermal decay curves, as shown in Fig. 13. $LaPO_4:0.005Eu^{3+},0.005Pr^{3+}$ with the most intense glow peak also shows the most intense afterglow.

For $LaPO_4:0.005Eu^{3+},0.005Tb^{3+}$ and $LaPO_4:0.005Eu^{3+},0.005Pr^{3+}$, we obtained afterglow from Eu^{3+} . Fig. 14 shows the TL emission (TLEM) spectra of $LaPO_4:0.005Yb^{3+},0.005Pr^{3+}$, where the emission was from Yb^{3+} at 1000 nm in the short wavelength infrared (SWIR) 900–1700 nm range. Additional TL emission plots for other $REPO_4$ with combinations of Yb^{3+} and Tb^{3+} or Pr^{3+} can be found in Fig. S4i–l, ESI,† and in each case, IR Yb^{3+} TL glow was observed. Infrared persistent luminescence from Yb^{3+} appeared in $LaPO_4:0.005Yb^{3+},0.005Pr^{3+}$ and $LaPO_4:0.005Yb^{3+},0.005Tb^{3+}$ at room temperature.

The room temperature afterglow of $LaPO_4:0.005Eu^{3+},0.005Tb^{3+}$ and $LaPO_4:0.005Eu^{3+},0.005Pr^{3+}$ was related to the lowest temperature glow peak. To study the origin of this glow peak, Fig. 15 shows the TL excitation (TLE) spectra of the low temperature glow peak at

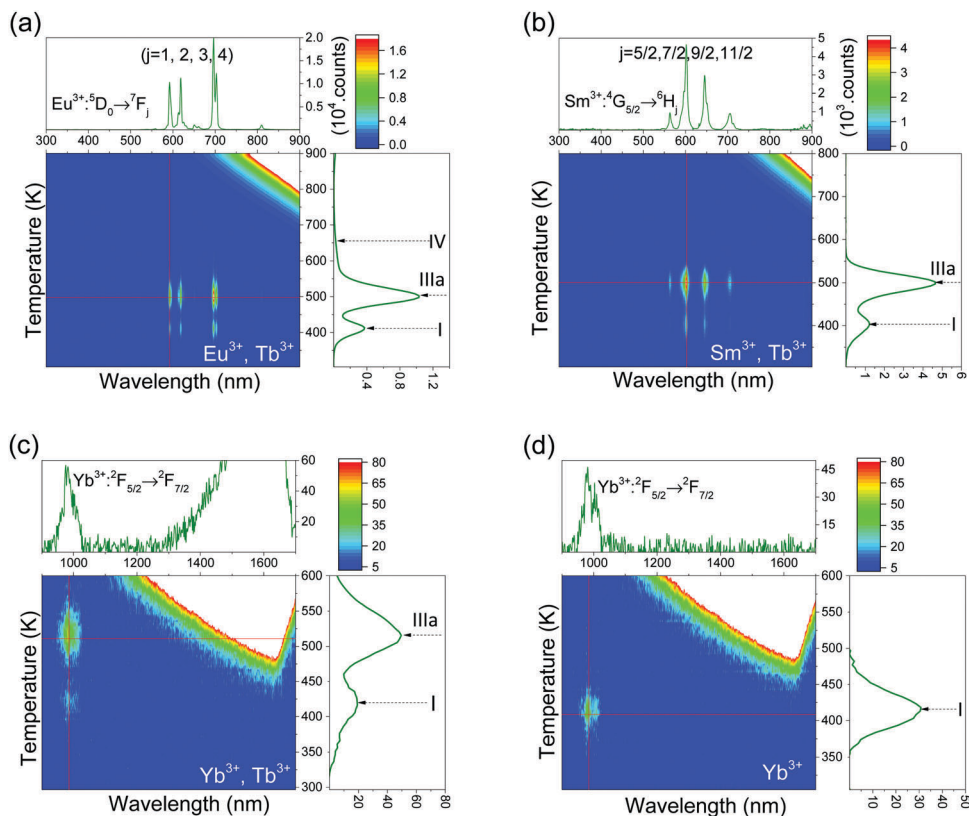


Fig. 8 Thermoluminescence emission (TLEM) spectra of (a) $\text{YPO}_4:0.005\text{Eu}^{3+},0.005\text{Tb}^{3+}$, (b) $\text{YPO}_4:0.005\text{Sm}^{3+},0.005\text{Tb}^{3+}$, (c) $\text{YPO}_4:0.005\text{Yb}^{3+},0.005\text{Tb}^{3+}$, and (d) $\text{YPO}_4:0.005\text{Yb}^{3+}$ at a heating rate of 1 K s^{-1} .

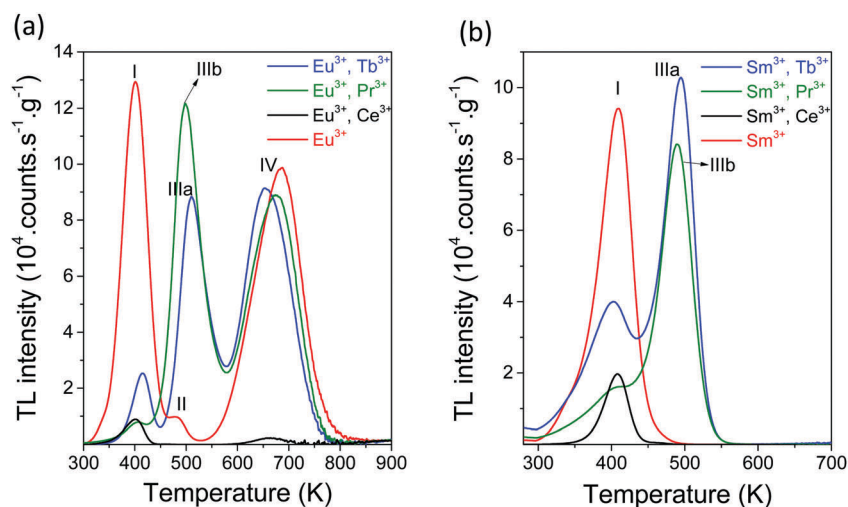


Fig. 9 TL glow curves of (a) $\text{YPO}_4:0.005\text{Eu}^{3+},0.005\text{Ln}^{3+}$ and (b) $\text{YPO}_4:0.005\text{Sm}^{3+},0.005\text{Ln}^{3+}$ recorded after 2000 s β source radiation monitoring the emission from Eu^{3+} or from Sm^{3+} at the heating rate of 1 K s^{-1} .

300–380 K of $\text{LaPO}_4:0.005\text{Eu}^{3+},0.005\text{Tb}^{3+}$. A broad TLE band ranging from 200 to 300 nm and peaking at 260 nm was observed. The width and position was similar to that of the photoluminescence excitation (PLE) spectra of Eu^{3+} single doped LaPO_4 (also shown in Fig. 15). This demonstrated that after Eu^{3+} CT-band excitation, the holes that were generated in the valence band were trapped by the defects responsible for the low temperature glow peak.

4. Discussion

The vacuum referred binding energy (VRBE) diagrams shown in Fig. 1 are first discussed; then we show how they can be used for tailoring the trapping and release process of electrons and holes in REPO_4 . The energy of an electron at rest in vacuum is defined as the reference energy, *i.e.*, zero point energy.¹⁸ VRBE

Table 3 TL results for $\text{REPO}_4:0.005\text{Ln}^{3+},\text{Tb}^{3+}$ or Pr^{3+} providing the trap depths E (eV) for the glow peaks IIIa and IIIb and frequency factor s (s^{-1})

Compound	s	Ln^{3+}	Tb E (IIIa)	Pr E (IIIb)
YPO_4	1.45×10^{13}	Eu^{3+}	1.45	1.41
YPO_4	1.45×10^{13}	Sm^{3+}	1.42	1.40
YPO_4	1.45×10^{13}	Yb^{3+}	1.46	1.46
$\text{Y}_{0.75}\text{Lu}_{0.25}\text{PO}_4$	4.45×10^{13}	Eu^{3+}	1.52	1.50
$\text{Y}_{0.5}\text{Lu}_{0.5}\text{PO}_4$	2.53×10^{14}	Eu^{3+}	1.65	1.63
$\text{Y}_{0.5}\text{Lu}_{0.5}\text{PO}_4$	2.53×10^{14}	Yb^{3+}	1.62	1.61
$\text{Y}_{0.25}\text{Lu}_{0.75}\text{PO}_4$	1.29×10^{15}	Eu^{3+}	1.78	1.75
LuPO_4	1.03×10^{15}	Eu^{3+}	1.84	1.80
LuPO_4	1.03×10^{15}	Yb^{3+}	1.79	1.78
LaPO_4	2.14×10^{12}	Eu^{3+}	0.63	0.55

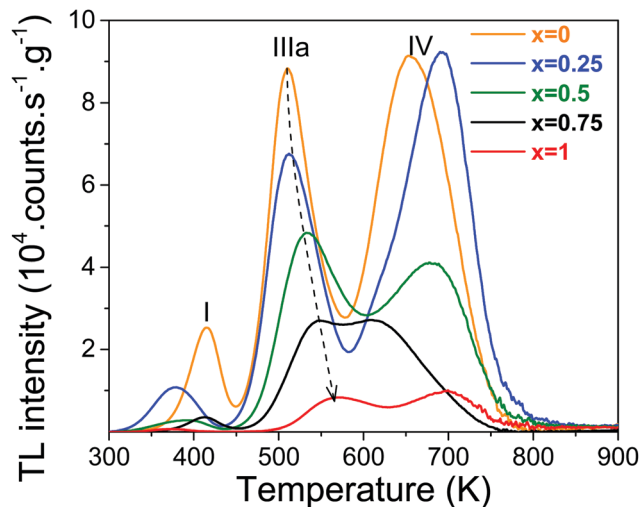


Fig. 10 TL glow curves for $\text{Y}_{1-x}\text{Lu}_x\text{PO}_4:0.005\text{Eu}^{3+},0.005\text{Tb}^{3+}$ solid solutions monitoring the red emission from Eu^{3+} at the heating rate of 1 K s^{-1} .

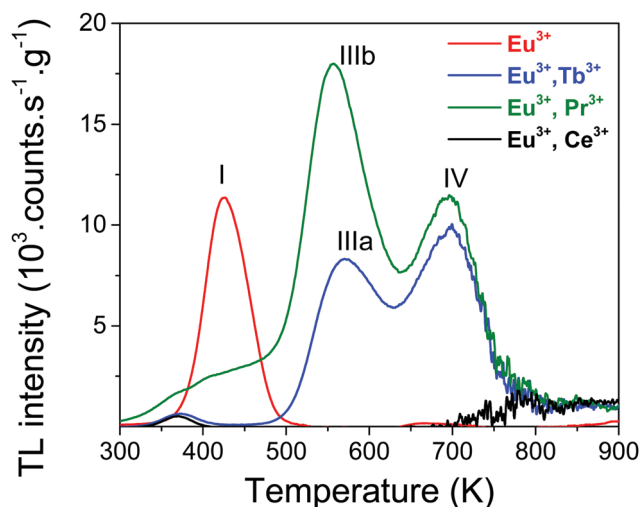


Fig. 11 TL glow curves for $\text{LuPO}_4:0.005\text{Eu}^{3+},0.005\text{Ln}^{3+}$ ($\text{Ln} = \text{Tb}, \text{Pr}, \text{and Ce}$) samples monitoring the red emission from Eu^{3+} at the heating rate of 1 K s^{-1} .

is defined as the energy needed to extract an electron from a system and bring it into vacuum.^{16,17} This electron can be from a host band or from an impurity ground or excited state.

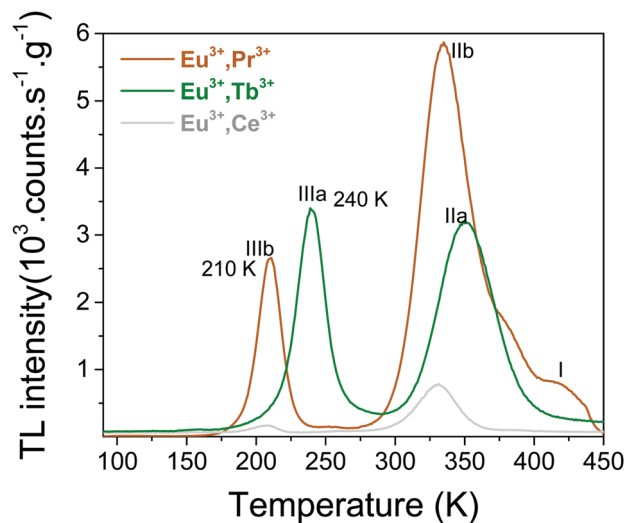


Fig. 12 TL glow curves for $\text{LaPO}_4:0.005\text{Eu}^{3+},0.005\text{Ln}^{3+}$ ($\text{Ln} = \text{Tb}, \text{Pr}, \text{and Ce}$) samples monitoring the Eu^{3+} emission in the temperature range of 90–450 K at the heating rate of 1 K s^{-1} .

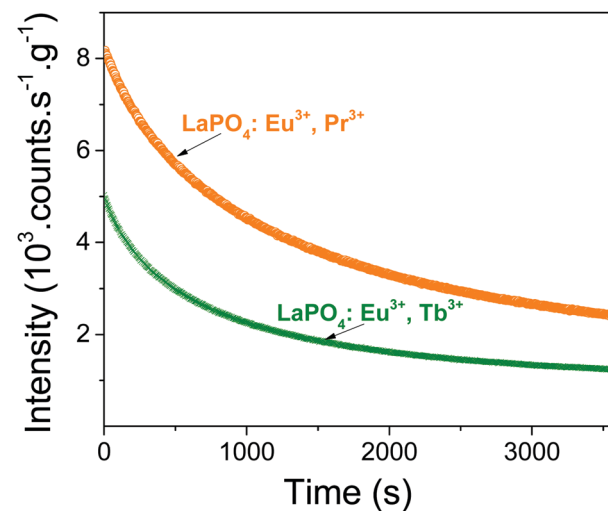


Fig. 13 Room temperature isothermal decay curves of $\text{LaPO}_4:0.005\text{Eu}^{3+},0.005\text{Tb}^{3+}$ and $\text{LaPO}_4:0.005\text{Eu}^{3+},0.005\text{Pr}^{3+}$. A 600 nm bandpass filter (600FS40-50) was used to monitor the red emission of Eu^{3+} .

To construct VRBE diagrams, one first needs the values for the U -parameter that are listed in column 2 of Table 4. The U -parameters are already derived for REPO_4 ($\text{RE} = \text{La}, \text{Y}$ and Lu) in ref. 22 and estimated for GdPO_4 . From these values the VRBE in the Eu^{2+} ground state is calculated with the chemical shift model and results are shown in column 3 of Table 4. The VRBE at the valence band top shown in column 5 can be obtained employing the $\text{VB} \rightarrow \text{Eu}^{3+}$ CT energy, as measured in Fig. 4 and given in column 4. The VRBE E_C at the conduction band bottom shown in column 7 of Table 4 is obtained from the host exciton creation energy E^{ex} in column 6 by adding the exciton binding energy estimated as $0.008(E^{\text{ex}})^2$ in ref. 19. We use the most recent parameter sets from ref. 19 to construct the double zigzag curves that provide the VRBE in divalent lanthanide

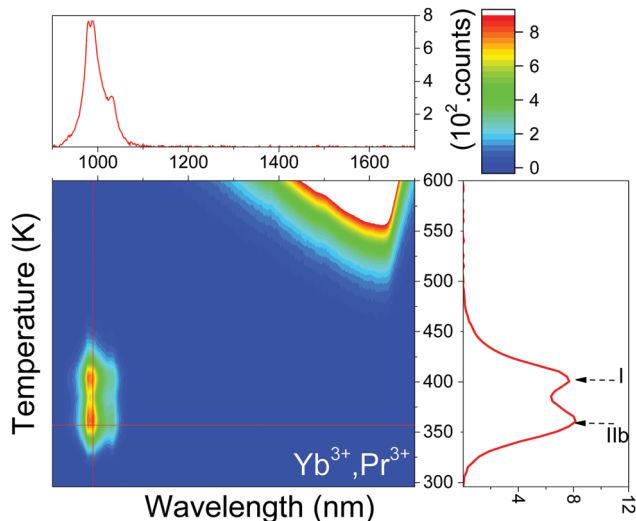


Fig. 14 TL emission (TLEM) spectra for $\text{LaPO}_4:0.005\text{Yb}^{3+},0.005\text{Pr}^{3+}$.

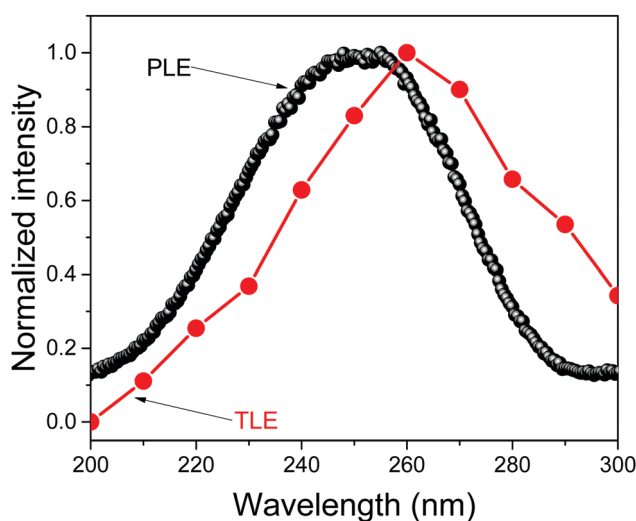


Fig. 15 Thermoluminescence excitation (TLE) spectra of $\text{LaPO}_4:0.005\text{Eu}^{3+},0.005\text{Tb}^{3+}$ and photoluminescence excitation (PLE) spectrum ($\lambda_{\text{em}} = 590 \text{ nm}$) of $\text{LaPO}_4:0.005\text{Eu}^{3+}$ performed at room temperature.

ground states and trivalent ground states, as listed for Tb and Pr in columns 8 and 9.

4.1. Electron trap depth tailoring via conduction band engineering

Fig. 5 shows that T_m strongly depends on the type of the lanthanide in $\text{LaPO}_4:0.005\text{Ce}^{3+},0.005\text{Ln}^{3+}$. A similar dependence

Table 4 Parameters used to establish the VRBE diagrams for REPO_4 (RE = La, Gd, Y, and Lu) in eV and the results from these diagrams

REPO_4	U	E_{Eu}^{2+}	$E_{\text{Eu}}^{3+,\text{CT}}$	E_{V}	E^{ex}	E_{C}	$E_{\text{Tb}^{3+}}$	$E_{\text{Pr}^{3+}}$
La	7.18	-4.16	4.84	-9.00	8.00	-0.49	-7.77	-7.95
Gd	7.15	-4.15	5.14	-9.28	8.05	-0.71	-7.73	-7.91
Y	7.09	-4.12	5.65	-9.77	8.55	-0.63	-7.64	-7.82
Lu	7.08	-4.11	5.74	-9.85	8.60	-0.66	-7.62	-7.80

has been reported for $\text{GdAlO}_3:0.01\text{Ce}^{3+},0.01\text{Ln}^{3+}$,⁷ $\text{Y}_3\text{Al}_5\text{O}_{12}:0.003\text{Ce}^{3+}/\text{Pr}^{3+}/\text{Tb}^{3+},0.003\text{Ln}^{3+}$,³⁴ and $\text{YPO}_4:0.005\text{Ce}^{3+},0.005\text{Ln}^{3+}$.³⁵ Using the derived electron trap depths listed in column 3 of Table 1, we place the Ln^{2+} ground state levels below the conduction band in the VRBE diagram of Fig. 16a. Apart from a deviation of 0.1–0.4 eV, the data from TL glow peak analysis follow the divalent lanthanide zigzag curve in the VRBE diagram.

Fig. 16b shows T_m from Fig. 5 for $\text{LaPO}_4:0.005\text{Ce}^{3+},0.005\text{Ln}^{3+}$ against the trap depths read from the VRBE diagram and against trap depths derived by TL glow peak analysis. Proportional relationships are observed with the slope $T_m/E = 355 \text{ K eV}^{-1}$ and 398 K eV^{-1} . Assuming first-order TL-recombination kinetics, eqn (1) can also be written as

$$\frac{T_m}{E} = \frac{11600}{\ln\left(\frac{T_m}{E}\right) + \ln\left(\frac{s}{\beta}\right) + \ln(T_m) - 9.36} \text{ K eV}^{-1} \quad (2)$$

The frequency factor s in inorganic compounds is typically 10^{13} s^{-1} and $\ln\left(\frac{s}{\beta}\right)$ is then 28.3 for $\beta = 5 \text{ K s}^{-1}$. $\ln\left(\frac{T_m}{E}\right)$ and $\ln(T_m)$ are both near 6, which implies that the value for the numerator in eqn (2) is about 31 and almost entirely determined by $\ln\left(\frac{s}{\beta}\right)$. It also implies that $\frac{T_m}{E}$ will be, to a good approximation, a constant with values of 300–400 K eV^{-1} depending on $\ln\left(\frac{s}{\beta}\right)$ as observed. Proportional relations were also reported for lanthanides in YPO_4 ,³⁵ CaSO_4 ,³⁶ and $\text{Sr}_3\text{Al}_x\text{Si}_{1-x}\text{O}_5$ ³⁷ with $T_m/E = 284 \text{ K eV}^{-1}$ at $\beta = 0.1 \text{ K s}^{-1}$, $T_m/E = 313 \text{ K eV}^{-1}$ at $\beta = 0.42 \text{ K s}^{-1}$, and $T_m/E = 322 \text{ K eV}^{-1}$ at $\beta = 0.1 \text{ K s}^{-1}$. Particularly, for YPO_4 , $T_m/E = 300 \text{ K eV}^{-1}$ was obtained at $\beta = 1 \text{ K s}^{-1}$. Fig. 11b also shows that the two fitted lines (a) and (b) deviate. Clearly, taking into account the error by VRBE and considering that there is an uncertainty in the slope of the line based on the thermoluminescence measurements as well, the trend is in accordance.

Fig. 2, which was obtained from the data of Table 4, shows the stacked vacuum referred binding energy (VRBE) diagram of REPO_4 with the VRBE in the $4f^7$ ground states of Pr^{3+} , Tb^{3+} , and Eu^{2+} . The VRBE diagrams with all lanthanide impurity level locations can be found in Fig. S9, ESI.† The conduction band bottom moves 0.22 eV downward with the substitution of La^{3+} by Gd^{3+} in $\text{Gd}_{1-x}\text{La}_x\text{PO}_4$ solid solutions (column 7 of Table 4) and then the Ln^{3+} electron trap depths decrease. This is consistent with the 105 K TL peak shift in Fig. 7a. The same sequence of TL glow peaks of the same Ln^{3+} dopant as in Fig. 5 is observed for $\text{YPO}_4:\text{Ce}^{3+},\text{Ln}^{3+}$ at the same heating rate of 5 K s^{-1} in ref. 35. All glow peaks in YPO_4 are shifted 90–100 K towards lower T_m , as shown in Fig. S10, ESI.† Assuming $T_m/E \sim 350 \text{ K eV}^{-1}$, this corresponds with 0.26 eV more shallow trap depth in YPO_4 , whereas Fig. 2 and Table 4 predict 0.18 eV more shallow trap depth.

From the almost 100 K broad TL glow peak observed for $x = 0.25$ in Fig. 7a, a 0.95–1.2 eV wide electron trap depth distribution is found (see Table 2). Apparently, the VRBE at the conduction band bottom shows site-to-site fluctuations

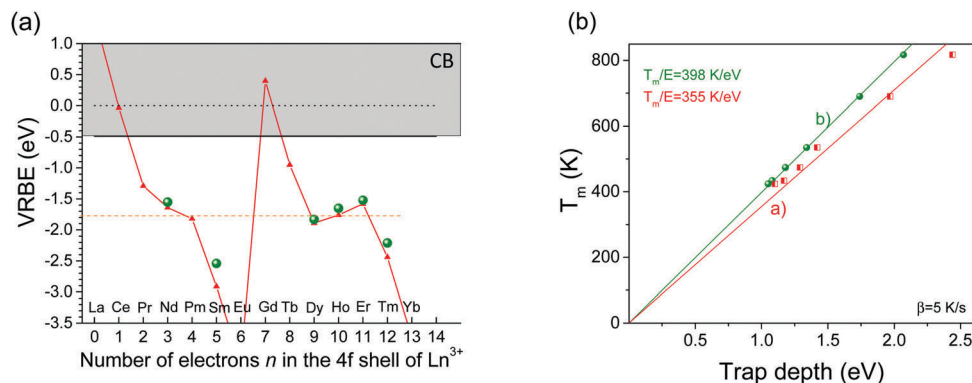


Fig. 16 (a) VRBE diagram for the divalent lanthanides in LaPO_4 (\blacktriangle) together with VRBE data from TL studies on $\text{LaPO}_4:0.005\text{Ce}^{3+}, 0.005\text{Ln}^{3+}$ (\bullet). (b) T_m against trap depth as line (a) determined from the VRBE diagram and line (b) from TL studies of $\text{LaPO}_4:0.005\text{Ce}^{3+}, 0.005\text{Ln}^{3+}$.

depending on the statistics in replacing La by Gd in the $\text{Gd}_{1-x}\text{La}_x\text{PO}_4$ solid solution at $x = 0.25$. A similar phenomenon is reported for Eu^{3+} -doped SnO_2 nanoparticles³⁸ and $\text{Y}_3\text{Al}_{5-x}\text{Ga}_x\text{O}_{12}:\text{Ce}^{3+}, \text{Cr}^{3+}$ solid solutions when changing the ratio of Ga^{3+} to Al^{3+} .¹³

4.2. Controlling hole trap depth

The vacuum referred binding energy (VRBE) diagrams of REPO_4 in Fig. 1 and Fig. S9, ESI[†] predict that the holes trapped by Tb^{4+} and Pr^{4+} are liberated earlier, *i.e.*, at lower temperature than the electrons trapped at Eu^{2+} , Yb^{2+} , and Sm^{2+} to generate the characteristic 4f–4f emission of Eu^{3+} , Yb^{3+} , and Sm^{3+} .

The room temperature TL excitation spectra for $\text{LaPO}_4:0.005\text{Eu}^{3+}, 0.005\text{Tb}^{3+}$ in Fig. 15 strongly resembles with the $\text{VB} \rightarrow \text{Eu}^{3+}$ CT band in Fig. 4, *i.e.*, the width is the same but it appears 10 nm red shifted, corresponding with 0.2 eV. During CT-band excitation, holes are generated in the valence band²⁷ and this is usually followed by the back transfer of the electron from Eu^{2+} , causing Eu^{3+} emission. Struck *et al.* reported on the phenomenon of hole separation from the Eu^{3+} CT state in $\text{RE}_2\text{O}_2\text{S}$ ($\text{RE} = \text{Y}^{3+}$ and La^{3+}) during Eu^{3+} CT excitation.³⁹ Dobrov *et al.* reported that a p-type photoconductivity signal was found in $\text{La}_2\text{O}_2\text{S}:\text{Eu}$ during the $\text{VB} \rightarrow \text{Eu}^{3+}$ CT excitation.⁴⁰ Therefore, during CT-band excitation, holes can be liberated from the CT state and subsequently migrate to hole trapping centers that can host intrinsic defects or intentional defects such as Tb^{3+} and Pr^{3+} . Fig. 15 suggests that this occurs in $\text{LaPO}_4:0.005\text{Eu}^{3+}, 0.005\text{Tb}^{3+}$ and the close to room temperature glow peak in Fig. 12 must be attributed to the release of holes from either Tb^{4+} or an intrinsic defect. The 0.2 eV red shift in band location may indicate that the hole trap is close to Eu^{3+} , thus facilitating hole release.

Fig. 8a–c shows TL emission (TLEM) spectra for YPO_4 with the same Tb^{3+} hole trapping center but with different deep electron trapping centers of Eu^{3+} , Sm^{3+} , and Yb^{3+} . All samples share TL glow peaks I and IIIa with emission from either Eu^{3+} , Sm^{3+} or Yb^{3+} . Peak IIIa is assigned to hole release from Tb^{4+} . Peak I is also observed when the Tb^{3+} hole trap is replaced by the Pr^{3+} or Ce^{3+} hole trap in the samples of Fig. 9 and Fig. S4, ESI[†]. We therefore attribute peak I to hole release from an unidentified host associated hole trap. Glow peak IV in Fig. 9a

is only observed in Eu^{3+} -doped samples and it seems to be a further unidentified hole trap somehow related to Eu presence.

Using data in columns 4 and 5 of Table 3, the average trap depths for Pr^{3+} and Tb^{3+} in YPO_4 are 1.42 and 1.44 eV, respectively, which are ~ 0.6 eV smaller than the ones predicted from the VRBE diagram (1.95 for Pr^{3+} and 2.13 eV for Tb^{3+}). A similar deviation was observed in GdAlO_3 .⁷ When holes are produced in the valence band, they tend to form a V_k center by bonding two neighbouring oxygen anions.^{41,42} In a VRBE diagram, such a V_k center level is located above the valence band top.^{7,43} We therefore attribute the 0.6 eV energy difference to the binding energy of the V_k center. Under thermal excitation, such a V_k center moves towards the electron trapped at Yb^{2+} , Sm^{2+} , or Eu^{2+} producing 4f–4f emission of Yb^{3+} , Sm^{3+} , or Eu^{3+} in YPO_4 .

4.3. Hole trap depth tailoring via valence band engineering

Since the VRBE in the Tb^{3+} and Pr^{3+} ground states in our phosphate compounds are about the same, the hole trap depths of Tb^{3+} and Pr^{3+} will depend on the VRBE at the valence band top (E_v). Therefore, one can tailor the T_m of glow peaks IIIa and IIIb by engineering the VRBE at the valence band top. The stacked diagram in Fig. 2 and column 5 in Table 4 show that E_v lowers by 0.85 eV in discrete steps in going from La to Gd to Y to Lu phosphate, and the hole trapping depths and T_m of peaks IIIa and IIIb should increase accordingly.

The results of the $\text{Y}_{1-x}\text{Lu}_x\text{PO}_4$ solid solutions in Fig. 10 and Fig. S7, ESI[†] demonstrate this tailoring. For both Tb and Pr, glow peaks IIIa and IIIb shift upward by about 65 K when replacing Y^{3+} by Lu^{3+} . Using the T_m/E relationship of typical 350 K eV^{-1} , this would imply a 0.2 eV deeper hole trap depth. From the variable heating rate plots for $\text{Y}_{1-x}\text{Lu}_x\text{PO}_4:0.005\text{Eu}^{3+}, 0.005\text{Tb}^{3+}$ in Fig. S6, ESI[†] about 0.4 eV deeper hole trapping depth is found. The VRBE results in Table 4 suggest only 0.1 eV larger trapping depth. This demonstrates the limitations of accurate measurement of trapping depths derived from TL glow curve analysis and VRBE diagram. The VRBE diagram, which is based on wide CT-band transitions and other experimental input parameters, can easily contain errors of several 0.1 eV size, and the same applies for results from TL data. For example,

for $\text{LaPO}_4:0.005\text{Ce}^{3+},0.005\text{Ho}^{3+}$, electron trap of 1.18 eV is found, but in column 3 of Table 2, for the same sample, a value of 1.22 eV is obtained. These differences are directly related to different values for the frequency factors. In this work, we analyzed the TL-glow peaks assuming first order recombination kinetics and with zero distribution in trapping depths. Such a situation is not realistic and reported trapping depth energies and frequency factors should be treated as indicative.

The VRBE diagram of LaPO_4 in Fig. 2 and Table 4 predicts that Eu^{3+} can act as a 3.67 eV deep electron trapping center, while Ce^{3+} , Tb^{3+} , and Pr^{3+} can act as 2.90, 1.23, and 1.05 eV shallow hole trapping centers. Considering that LaPO_4 and YPO_4 are quite similar, we assume that the binding energy of the V_k center in LaPO_4 is 0.6 eV, like in YPO_4 . We then arrive at effective hole trapping depths of 2.30, 0.63, and 0.45 eV for Ce^{3+} , Tb^{3+} , and Pr^{3+} , respectively. One can estimate according to eqn (1) with a heating rate of 1 K s^{-1} and the above predicted trapping depths that hole release from Ce^{4+} , Tb^{4+} , and Pr^{4+} in LaPO_4 give glow peaks at $T_m \sim 840$, 240, and 170 K, respectively. Clearly, the Ce^{4+} trap is far too deep to release a hole in the measurement range. In contrast, the predicted T_m values for Tb^{4+} and Pr^{4+} hole release are in the range of the appearance of glow peaks IIIa (0.63 eV) and IIIb (0.55 eV) in Fig. 12. We therefore tentatively attribute glow peaks IIIa and IIIb to hole release from Tb^{4+} and Pr^{4+} . The intense glow peak just above RT is then assigned to intrinsic hole traps.

The VRBE diagram for LaPO_4 , and GdPO_4 in Fig. 2 and the data in Table 4 suggests that Tb^{3+} and Pr^{3+} hole trap depth increase by about 0.3 eV, corresponding to the about 100 K shift in T_m . The glow peak maxima are then expected to be between 300 and 400 K in GdPO_4 . TL glow curves for $\text{GdPO}_4:0.005\text{Eu}^{3+},0.005\text{Ln}^{3+}$ ($\text{Ln} = \text{Tb}, \text{Pr}, \text{and Ce}$) samples indeed show glow peaks between 300 and 400 K in Fig. S11, ESI†. However, since these glow peaks are also present with Ce^{3+} co-doping and for single Eu^{3+} samples, they cannot be assigned to either Tb or Pr . This also applies to $\text{GdPO}_4:0.005\text{Sm}^{3+},0.005\text{Ln}^{3+}$.

The data in Table 4 from the VRBE diagram places the ground state level of $\text{Tb}^{3+} \sim 0.18 \text{ eV}$ higher than that of Pr^{3+} and release of holes from Tb^{4+} occur 60–70 K higher than from Pr^{4+} . However, Fig. 9, 11, and 12 show that the Pr^{4+} TL glow peak appears at 10–30 K lower temperature than that of Tb^{4+} in Y -, Lu -, and LaPO_4 . For GdAlO_3 it was found in ref. 7 that the Pr^{4+} glow peak is at 10–30 K higher than that of the Tb^{4+} . Based on these observations, it seems that the ground states of Tb^{3+} and Pr^{3+} have in those compounds about the same VRBE value. It provides a hint that the parameter values behind the trivalent lanthanide zigzag curve in the VRBE diagrams need adjustment or otherwise might be slightly compound dependent.

There is an increasing need for afterglow phosphors that exhibit emission in the short-wave infrared (SWIR) spectral region of ~ 900 – 1700 nm owing to many advanced applications in the field of military, anti-counterfeiting, and bio-imaging.⁴⁴ For instance, for military utilizations, the SWIR light is more mysterious than near-infrared light, which cannot be easily probed by conventional techniques such as night-vision spectacles. For bio-imaging, SWIR light is located in the second

biological window (~ 1000 – 1400 nm), allowing ultra-sensitive and deep-tissue bio-imaging.¹⁰ However, few SWIR phosphors have been developed since it remains unclear how to design this type of materials.⁴⁵

SWIR afterglow can be realized by replacing Eu^{3+} for Yb^{3+} and combining that with Tb^{3+} or Pr^{3+} in La , Y , Gd , and Lu phosphates or in solid solutions thereof. The VRBE at the VB top and therewith the Tb^{3+} and Pr^{3+} hole trap depths can then be engineered. The results on the $\text{Yb}^{3+},\text{Tb}^{3+}$ -codoped YPO_4 in Fig. 8c, $\text{Y}_{1-x}\text{Lu}_x\text{PO}_4$ solid solution in Fig. S4i, and LuPO_4 in Fig. S4j, ESI† demonstrate such engineering.

5. Conclusions

The chemical shift model, photoluminescence spectroscopy and thermoluminescence have been combined to study the trapping and release process of electrons and holes in double lanthanide doped rare earth ortho phosphates. In $\text{LaPO}_4:0.005\text{Ce}^{3+},0.005\text{Ln}^{3+}$, the Ln^{3+} codopants act as electron trapping centers, while Ce^{3+} acts as the luminescence center. The electrons liberated from Ln^{2+} recombine with Ce^{4+} yielding Ce^{3+} 5d–4f emission. The electron trap depth generated by lanthanide codopants can be tuned by the choice of Ln^{3+} , and for fixed set of lanthanide dopants like in $\text{Gd}_{1-x}\text{La}_x\text{PO}_4:0.005\text{Ce}^{3+},0.005\text{Ho}^{3+}$ solid solutions, by tuning x , leading to conduction band engineering. For $\text{YPO}_4:0.005\text{Ln}^{3+},0.005\text{M}^{3+}$ ($\text{Ln} = \text{Sm}, \text{Eu}, \text{and Yb}; \text{M} = \text{Pr} \text{ and } \text{Tb}$), Ln^{3+} acts as the electron trapping center and recombination center, while M^{3+} acts as the hole trapping center. Compared with electrons trapped at Ln^{2+} , holes trapped by M^{4+} liberate at a lower temperature and recombine with Ln^{2+} to produce Ln^{3+} 4f–4f emission during the TL readout. VRBE at the valence band top can be engineered through the substitution of Y^{3+} by Lu^{3+} or La^{3+} and this enables the tailoring of hole trap depths of Tb^{3+} and Pr^{3+} , and the emitting wavelength can be tailored from red to SWIR by changing the electron traps from Eu^{3+} or Sm^{3+} to Yb^{3+} . Particularly, new SWIR afterglow phosphors with Yb^{3+} infrared emission in ~ 900 – 1700 nm have been discovered by tuning the hole trap depth in the ortho phosphates. With the deep understanding of trap level locations and about the transport and trapping processes of charge carriers, such conduction and valence band engineering can be a promising route to deliberately design the electron and hole trap based novel optical storage and persistent phosphors.

Conflicts of interest

There are no conflicts to declare.

Acknowledgements

T. Lyu acknowledges the Chinese Scholarship Council for his PhD scholarship (Tianshuai Lyu: No. 201608320151). We thank Dr Adrie J. J. Bos and Dr Hongde Luo from Delft University of

Technology for fruitful discussions on afterglow phosphors and luminescence mechanisms.

References

- 1 Y. Li, M. Gecevicius and J. Qiu, *Chem. Soc. Rev.*, 2016, **45**, 2090–2136.
- 2 H. Luo, A. J. J. Bos and P. Dorenbos, *J. Phys. Chem. C*, 2017, **121**, 8760–8769.
- 3 T. Wang, W. Bian, D. Zhou, J. Qiu, X. Yu and X. Xu, *J. Phys. Chem. C*, 2015, **119**, 14047–14055.
- 4 Y. Zhuang, Y. Katayama, J. Ueda and S. Tanabe, *Opt. Mater.*, 2014, **36**, 1907–1912.
- 5 P. Leblans, D. Vandenbroucke and P. Willems, *Materials*, 2011, **4**, 1034.
- 6 Y. Wang, Y. Gong, X. Xu and Y. Li, *J. Lumin.*, 2013, **133**, 25–29.
- 7 H. Luo, A. J. J. Bos and P. Dorenbos, *J. Phys. Chem. C*, 2016, **120**, 5916–5925.
- 8 A. Jain, A. Kumar, S. J. Dhoble and D. R. Peshwe, *Renewable Sustainable Energy Rev.*, 2016, **65**, 135–153.
- 9 H. Guo, Y. Wang, G. Li, J. Liu, P. Feng and D. Liu, *J. Mater. Chem. C*, 2017, **5**, 2844–2851.
- 10 J. Xu, S. Tanabe, A. D. Sontakke and J. Ueda, *Appl. Phys. Lett.*, 2015, **107**, 081903.
- 11 Z. Pan, Y.-Y. Lu and F. Liu, *Nat. Mater.*, 2012, **11**, 58–63.
- 12 J. Ueda, M. Katayama, K. Asami, J. Xu, Y. Inada and S. Tanabe, *Opt. Mater. Express*, 2017, **7**, 2471–2476.
- 13 J. Ueda, P. Dorenbos, A. J. J. Bos, K. Kuroishi and S. Tanabe, *J. Mater. Chem. C*, 2015, **3**, 5642–5651.
- 14 K. Korthout, K. Van den Eeckhout, J. Botterman, S. Nikitenko, D. Poelman and P. F. Smet, *Phys. Rev. B: Condens. Matter Mater. Phys.*, 2011, **84**, 085140.
- 15 K. Chakrabarti, V. K. Mathur, J. F. Rhodes and R. J. Abbundi, *J. Appl. Phys.*, 1988, **64**, 1363–1366.
- 16 P. Dorenbos, *Phys. Rev. B: Condens. Matter Mater. Phys.*, 2012, **85**, 165107.
- 17 P. Dorenbos, *J. Mater. Chem.*, 2012, **22**, 22344–22349.
- 18 P. Dorenbos, *ECS J. Solid State Sci. Technol.*, 2013, **2**, R3001–R3011.
- 19 P. Dorenbos, *Opt. Mater.*, 2017, **69**, 8–22.
- 20 P. Dorenbos and E. G. Rogers, *ECS J. Solid State Sci. Technol.*, 2014, **3**, R150–R158.
- 21 P. Dorenbos, *J. Lumin.*, 2014, **151**, 224–228.
- 22 P. Dorenbos, *J. Phys.: Condens. Matter*, 2013, **25**, 225501.
- 23 P. Dorenbos, *J. Lumin.*, 2013, **136**, 122–129.
- 24 A. J. J. Bos, R. M. van Duijvenvoorde, E. van der Kolk, W. Drozdowski and P. Dorenbos, *J. Lumin.*, 2011, **131**, 1465–1471.
- 25 V. S. Levushkina, D. A. Spassky, E. M. Aleksanyan, M. G. Brik, M. S. Tretyakova, B. I. Zadneprovski and A. N. Belsky, *J. Lumin.*, 2016, **171**, 33–39.
- 26 P. Dorenbos, *J. Lumin.*, 2005, **111**, 89–104.
- 27 E. Nakazawa and F. Shiga, *J. Lumin.*, 1977, **15**, 255–259.
- 28 R. Chen and S. A. A. Winer, *J. Appl. Phys.*, 1970, **41**, 5227–5232.
- 29 W. Hoogenstraaten, *Philips Res. Rep.*, 1958, **13**, 515–693.
- 30 R. R. Haering and E. N. Adams, *Phys. Rev.*, 1960, **117**, 451–454.
- 31 A. J. J. Bos, *Radiat. Meas.*, 2006, **41**, S45–S56.
- 32 A. J. J. Bos, P. Dorenbos, A. Bessière and B. Viana, *Radiat. Meas.*, 2008, **43**, 222–226.
- 33 K. Van den Eeckhout, A. J. J. Bos, D. Poelman and P. F. Smet, *Phys. Rev. B: Condens. Matter Mater. Phys.*, 2013, **87**, 045126.
- 34 F. You, A. J. J. Bos, Q. Shi, S. Huang and P. Dorenbos, *Phys. Rev. B: Condens. Matter Mater. Phys.*, 2012, **85**, 115101.
- 35 A. J. J. Bos, P. Dorenbos, A. Bessière, A. Lecointre, M. Bedu, M. Bettinelli and F. Piccinelli, *Radiat. Meas.*, 2011, **46**, 1410–1416.
- 36 K. S. V. Nambi, V. N. Bapat and A. K. Ganguly, *J. Phys. C: Solid State Phys.*, 1974, **7**, 4403–4415.
- 37 H. Luo, A. J. J. Bos, A. Dobrowolska and P. Dorenbos, *Phys. Chem. Chem. Phys.*, 2015, **17**, 15419–15427.
- 38 J. Kong, W. Zheng, Y. Liu, R. Li, E. Ma, H. Zhu and X. Chen, *Nanoscale*, 2015, **7**, 11048–11054.
- 39 C. W. Struck and W. H. Fonger, *Phys. Rev. B: Solid State*, 1971, **4**, 22–34.
- 40 W. I. Dobrov and R. A. Buchanan, *Appl. Phys. Lett.*, 1972, **21**, 201–203.
- 41 P. W. Tasker and A. M. Stoneham, *J. Phys. Chem. Solids*, 1977, **38**, 1185–1189.
- 42 R. B. Murray and F. J. Keller, *Phys. Rev.*, 1965, **137**, A942–A948.
- 43 N. F. Mott and A. M. Stoneham, *J. Phys. C: Solid State Phys.*, 1977, **10**, 3391.
- 44 F. Liu, Y. Liang, Y. Chen and Z. Pan, *Adv. Opt. Mater.*, 2016, **4**, 562–566.
- 45 Y. Liang, F. Liu, Y. Chen, X. Wang, K. Sun and Z. Pan, *J. Mater. Chem. C*, 2017, **5**, 6488–6492.